Richtmyer-Meshkov instability of a flat interface subjected to a rippled shock wave

Liyong Zou,* Jinhong Liu, Shenfei Liao, and Xianxu Zheng
Laboratory for Shock Wave and Detonation Physics, Institute of Fluid Physics, China Academy of Engineering Physics, P.O. Box 919-103, Mianyang, Sichuan 621900, China

Zhigang Zhai and Xisheng Luo
Department of Modern Mechanics, University of Science and Technology of China, Hefei 230026, China
(Received 31 August 2016; published 11 January 2017)

The Richtmyer-Meshkov (RM) instability of a nominally flat interface (N_2/SF_6) subjected to a rippled shock, as the counterpart of a corrugated interface interacting with a planar shock, is studied experimentally in a vertical shock tube using both schlieren photography and fog visualization diagnostics. The nonplanar incident shock wave is produced by a planar shock diffracting around a rigid cylinder, and the flat interface is created by a membraneless technique. Three different distances η (the ratio of spacing from cylinder to interface over cylinder diameter) are considered. Schlieren images indicate that the nonplanar incident shock can be divided into three different segments separated by two triple points. Fog visualization pictures show the formation of overall "Λ" shaped interface structures and a N_2 cavity at the center and two interface steps at both sides. With the increase of the dimensionless time, the dimensionless interface amplitude increases as well as the penetration depth of the cavity, and both curves exhibit reasonable collapse for different η numbers. Through equating the preinterface perturbation of the rippled shock with a preshock perturbation of a corrugated interface, the growth rate of this instability is found to be noticeably smaller than that of the standard RM instability.

DOI: 10.1103/PhysRevE.95.013107

I. INTRODUCTION

The Richtmyer-Meshkov instability (RM) instability arises when a shock wave impinges on a corrugated interface between two fluids with different properties [1]. This problem derives its name from pioneering work of Richtmyer [2] and subsequent confirmatory experiment by Meshkov [3]. Accompanied with vorticity deposition and transport, the RM instability alters the interface morphology and eventually the flow field enters a state of turbulent mixing. This phenomenon occurs in many important scientific areas such as astrophysics [4], supersonic combustion [5], and inertial confinement fusion [6], and has become increasingly significant in recent decades.

During the development of the RM instability, two primary mechanisms are responsible for the perturbation evolution. One is pressure perturbation caused by the shock behaviors such as shock reflection, diffraction, focusing, diverging, and shock-shock interaction [7,8]. The other is baroclinic vorticity induced by the misalignment of the density and pressure gradients ($\nabla\rho \times \nabla p \neq \mathbf{0}$ with $\nabla\rho$ the density gradient across the interface and ∇p the pressure gradient resulting from the shock wave) [9,10]. Generally, a planar shock wave for generating pressure gradient and an initial perturbed interface for providing density gradient are involved in most experimental studies of the RM instability for the easy implementation. Over the past decades, extensive investigations have been performed and fruitful advancements have been achieved on this problem from experiments [11–16], theoretical analysis [17–20], and numerical simulations [21–24]. Besides, a uniform converging shock wave interacting with a perturbed interface also has received much attention in recent years [25–29]. As the counterpart of a corrugated interface interacting with a planar shock, the RM instability will also occur when a nonuniform shock wave collides with a uniform interface. Actually, nonuniform shock waves widely exist in many scientific fields, such as inertial confinement fusion where the rippled shock wave is generated by the nonuniform laser irradiation, and it is therefore of fundamental interest to investigate the interaction of a rippled shock wave with a uniform interface. It is expected that the nonuniform flow induced by the rippled shock will have an important influence on the instability development. However, to the best of the authors' knowledge, experimental work on a nonuniform shock accelerating a uniform interface is seldom carried out in a shock tube environment.

In the present study, we shall report an experiment associated with a nonplanar shock hitting a nominally flat interface. The nonplanar shock wave is generated by the diffraction of a planar shock wave propagating over a rigid cylinder in a vertical shock tube. The initial flat interface is formed in the test section of the shock tube by a membraneless method. Two kinds of diagnostic techniques, high-speed schlieren and fog visualization, are implemented to capture the incident wave pattern and interface development during the shock-interface interaction. Three cases with different normalized distances η (the ratio of spacing from cylinder to interface over cylinder diameter) are experimentally investigated and the corresponding evolution processes are identified and analyzed.

II. EXPERIMENTAL METHODS

Experiments are conducted in a vertical shock tube IFP-V100 which consists of a 1.60-m-long driver section, a 4.22-m-long driven section, and a 0.31-m-long test section with a square cross-sectional area of 100 mm × 100 mm. Figure 1 depicts the sketch of the experimental facility in detail. The initial temperature and pressure in the driver and driven sections are 293 K and 101 325 Pa, respectively. Air is adopted

*liyong.zou@hotmail.com

 ©2017 American Physical Society

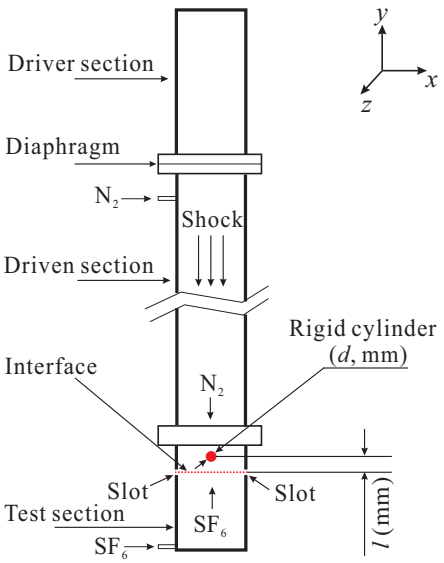

FIG. 1. Sketch of the vertical shock tube showing the nonplanar incident shock formation and the technique to create the initial planar interface. d, cylinder diameter; l, distance from the center of the cylinder to the interface.

as the driver gas and N_2 as the driven gas. Three pressure transducers (PCB M113A26) are mounted in the tube wall to measure the velocity of initial planar incident shock and trigger the optical system. The Mach number of the planar incident shock wave is 1.22 ± 0.01. All the experimental results are acquired during the effective experimental duration prior to the arrival of the reflected shock from the end wall of the tube or the reflected rarefaction wave from the driver section.

The nonplanar shock wave is created by the diffraction of a planar shock wave around a rigid cylinder in the vertical shock tube. Specifically, a circular PVC cylinder with diameter d is fixed in the test section. After the initial planar shock wave diffracts around the rigid cylinder, it becomes nonplanar. The technique to create an initial flat interface here is similar to the method applied in the related literature [30,31]. The light gas (N_2) and heavy gas (SF_6) are introduced into the shock tube very slowly from the top of the driven section and the bottom of the test section, respectively. The two opposing gas flows meet at the top of the test section and exit through two narrow slots on the opposite side walls, forming an initial planar interface. It should be mentioned that due to the small velocities of the two opposing gas flows in the shock tube ($\approx$0.8 cm/s) and large density ratio ($\approx$5) of two gases, a planar and stable interface at the slot position can be guaranteed. The flat interface is located at a distance l from the center of the cylinder, and this distance determines the shape of the nonuniform shock wave when it encounters the flat interface. In the present work, in order to demonstrate the influence of the rigid cylinder diameter (d) and the distance of the cylinder with the interface (l) on the shape of the nonuniform shock wave and on the evolution of the flat interface, two rigid cylinders with different diameters and two distances of the cylinder with the flat interface are, respectively, considered, as listed in Table I, in which $\eta = l/d$ is a dimensionless distance, varying from 2.0 to 4.0.

TABLE I. Experimental parameters for cases.

Case	d (mm)	l (mm)	$\eta\ (=l/d)$
1	10	20	2.0
2	6	20	3.3
3	10	40	4.0

In order to capture the evolution of the wave pattern and the initial interface, a schlieren system composed of a slit, a blade, two lenses, and two concave mirrors with diameter 300 mm is first adopted. As shown in Fig. 2(a), a 500-W xenon lamp (XQW500, Chengdu Photoelectricity Limited) is used as a continuous light source to illuminate the flow field, and a high-speed video camera (Photron FASTCAM) with a frame rate of 6×10^3 fps is used to capture the flow field through two 300 mm $\times$ 100 mm transparent glass windows mounted in the test section. The exposure time of the camera is 1 μs and the spatial resolution of the image is 0.27 mm/pixel. For examining the fine interface structure, fog visualization technique coupled with laser sheet is further employed to collect a series of dynamic images, as indicated in Fig. 2(b). The heavy gas (SF_6) is seeded with smoke fog (nominally 0.5 μm in diameter) as tracer particles. The flow field is illuminated by a Nd:YAG pulsed laser that provides 30 pulses with a frequency of 10 kHz ($\approx$100 mJ/pulse at a wavelength of 532 nm), and with a pulse duration of 10 ns. Through a set of lenses and reflectors, the cylindrical laser beam (SGR-Extra, Beamtech Limited) is transformed into a vertical laser sheet (with a thickness of $\sim$1 mm) which enters the test section

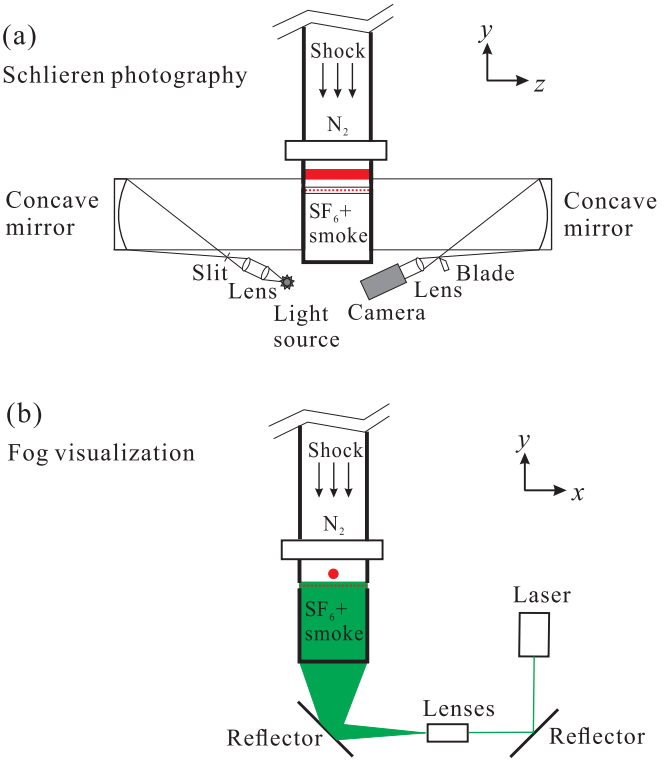

FIG. 2. Schlieren photography (a) and fog visualization diagnostics (b).

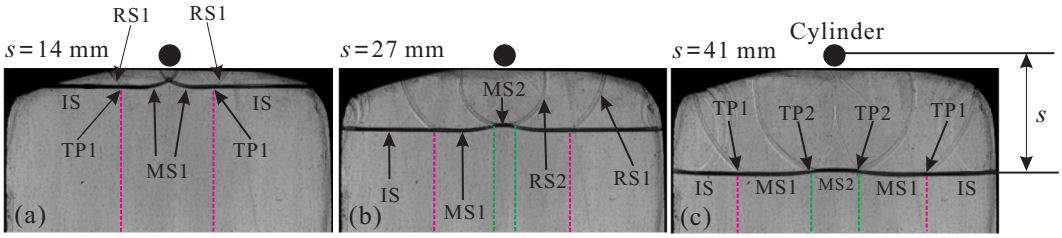

FIG. 3. Schlieren pictures displaying the wave pattern after the planar shock wave diffracts around a 10-mm-diameter rigid cylinder, The initial shock propagates from top to bottom, and s denotes the distance from the cylinder to the planar incident shock front. IS, incident shock; RS, reflected shock; TP, triple point; MS, Mach stem.

through the glass window embedded in the end wall of the shock tube. The evolving sequences during the postshock flow are captured with a Photron FASTCAM camera which is orthogonal to the laser sheet plane. The frame rate of the camera is 10^4 fps, and the spatial resolution of the image is 0.15 mm/pixel.

III. RESULTS AND DISCUSSION

Figure 3 presents schlieren images of the wave pattern after the planar shock wave diffracts around a rigid cylinder with a diameter of 10 mm. Initially, because the incident angle (the angle of the planar incident shock front with the cylinder surface) is small enough, regular reflection occurs accompanied by a reflected shock wave (RS). As the incident shock moves along the cylinder surface, the incident angle increases, and Mach reflection with a Mach stem occurs. When the incident shock moves downward further, two Mach stems at both sides of the cylinder will encounter at the downstream pole and collide with each other. As shown in Fig. 3(a), shortly after the shock departs from the downstream pole of the cylinder, the shock wave pattern is composed of the incident shock (IS), the first reflected shock (RS1), the first Mach stem (MS1), and the shocks caused by the collision of the MS1 (here we call these shocks RS2). At this moment, the two Mach stems nearly intersect at a point in the x-y plane. With the shocks moving downward, the reflected shocks RS1 and RS2 decrease in strength, and the curvature of the Mach stem also decreases. At this time, the original intersection point between the two Mach stems becomes a line in the x-y plane (we call this shock MS2), as shown in Fig. 3(b). The nonplanar incident shock can be divided into three different segments (IS, MS1, and MS2) separated by two triple points (TP1 and TP2). The second Mach stem MS2 is nearly planar and increases in length gradually, while the Mach stem MS1 still has a small curvature, as indicated in Fig. 3(c). Finally, the curved incident shock becomes planar. Therefore, the distance between the cylinder and the initial interface determines the shape of the rippled incident shock when it meets the interface, and consequently the evolution of the shocked interface.

Figure 4 gives the shapes of the initial interface and the rippled incident shock for three cases immediately before the shock accelerates the interface. From the schlieren images shown in Fig. 4(a), it is observed that the incident shock is distinctly nonplanar while the initial interface only has a large wavelength curvature. This means that the interface does not have any high wave number disturbance and, in all likelihood, its response to a cusped shock wave is very close to a flat interface case. Quantitative shapes of the nonplanar incident shock front, extracted from the schlieren images without considering the reflected shock, are indicated in Fig. 4(b). Similar to a perturbed single-mode interface, for the rippled shock wave, the initial amplitude (a_0) and width (W_0) are defined as the total height and extent of the rippled shock,

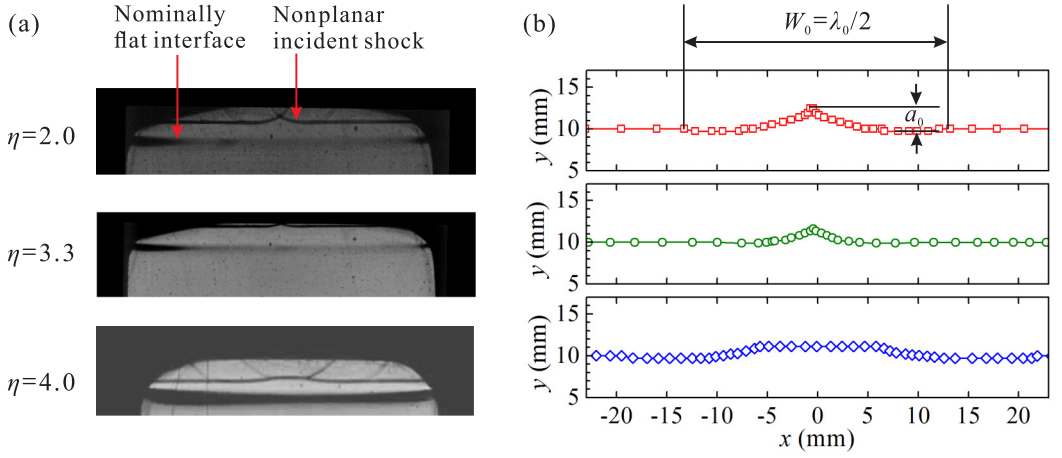

FIG. 4. (a) Schlieren pictures showing the shapes of the rippled incident shock and the interface. (b) Quantitative shape of the incident shock front extracted from the schlieren images. a_0, initial amplitude of rippled shock; W_0, initial width of rippled shock; λ_0, initial wavelength of rippled shock.

TABLE II. Amplitude (a_0) and wavelength (λ_0) of incident nonplanar shock.

Case	η	a_0 (mm)	λ_0 (mm)	a_0/λ_0
1	2.0	2.8	52.8	0.05
2	3.3	1.6	39.3	0.04
3	4.0	1.5	79.6	0.02

respectively. Accordingly, the initial wavelength (λ_0) of the rippled shock is taken as $\lambda_0 = 2W_0$. For these three cases, the initial amplitude and wavelength of the rippled shock are listed in Table II, from which one can observe that for each case the ratio of initial amplitude a_0 to wavelength λ_0 is less than 0.1 ($a_0/\lambda_0 < 0.1$). Moreover, with the increase of the dimensionless distance η, the initial amplitude a_0 decreases from 2.8 to 1.5 mm while λ_0 first decreases and then increases due to the smallest cylinder diameter d in case 2 and the largest propagation distance l in case 3.

Evolving sequences of the shocked interface using fog visualization technique are illustrated in Fig. 5. The initial time is defined as the moment when the incident shock contacts the interface. It should be noted that images before 1.8 ms are not available owing to the limitation of the window sizes of the high speed camera. Thus, the evolving images start at 1.8 ms and end at 2.5 ms, and the time interval is 0.1 ms. For each case, as shown in Fig. 5, the interface shape overall behaves like a "Λ" structure. It is easily found that a notable N_2 cavity in the middle part of the interface as indicated by solid circles in the images, and two interface steps on both sides of the cavity as highlighted by dashed circles, are generated. Evidently, from Fig. 5, we can notice that as η increases, the penetration depth of the cavity decreases while the area of the cavity increases. Especially, for $\eta = 4.0$, the cavity is even not closed.

Figure 6 qualitatively depicts the variation of the pressure (p) behind the nonuniform shock and the angle of the shock front with the interface (θ) for illustrating the cavity formation and interface morphology. In the first planar segment (IS), the incident shock and the initial interface are both uniform, thus the shocked interface keeps a planar shape. At the location

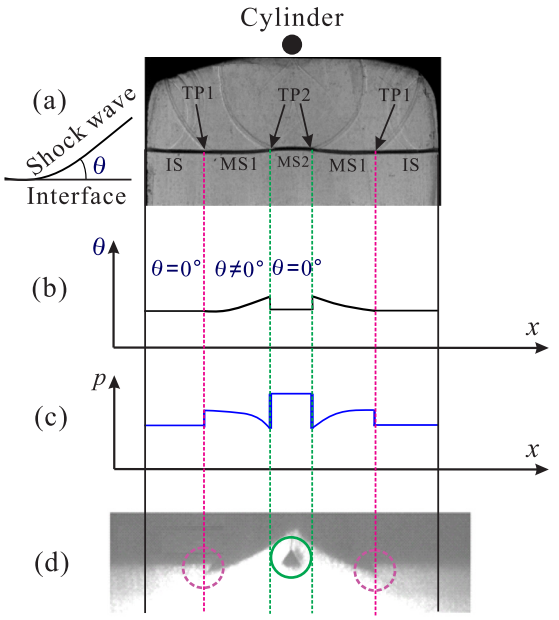

FIG. 6. (a) Shape of the rippled incident shock wave; (b) schematic of the incident angle (θ) of the shock front with the interface; (c) schematic of the pressure (p) distribution behind the rippled incident shock wave; (d) corresponding fog visualization image.

of TP1, note that when a planar shock wave moves along a rigid cylinder, the strength of Mach stem is stronger than that of the incident shock wave if Mach reflection occurs. Therefore, two interface steps appear due to the pressure jump resulting from the interaction of IS with RS1. In the curved segment (MS1), as the Mach stem diffracts along the cylinder, the strength of the Mach stem decreases gradually from TP1 to the cylinder. Thus the planar interface is accelerated by an approximately inclined shock wave with the shock strength decaying. Due to the small incident angle, vorticity magnitude induced by baroclinic torque in this segment is limited, and has very little influence on the interface morphology. As a result, the evolving interface in the curved segment has a similar

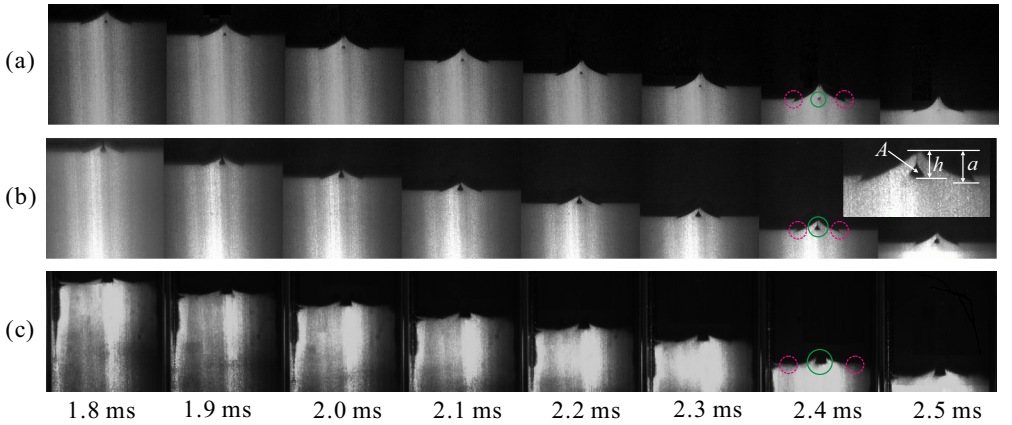

FIG. 5. Fog visualization sequences showing the evolution of the planar interface impacted by the rippled shock for $\eta = 2.0$ (a), $\eta = 3.3$ (b), and $\eta = 4.0$ (c). Solid circles indicate the N_2 cavity and dashed circles indicate the steps. a: amplitude from top to bottom of the interface; h: height from top of the interface to bottom of the cavity; A: area of the cavity.

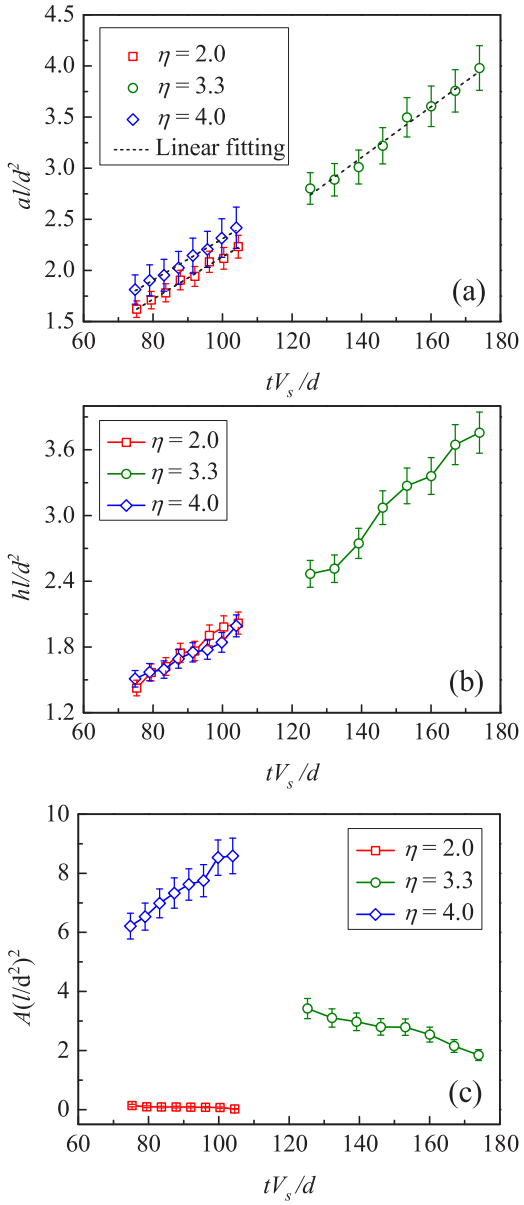

FIG. 7. Time variation of the dimensionless geometrical sizes of the distorted interface for three cases. (a) Amplitude from top to bottom of the interface; (b) height from top of the interface to bottom of the cavity; (c) area of the cavity.

shape to the shock wave, but may own a larger curvature than the shock wave because the shock strength is nonuniform. In the second planar segment (MS2), the collision of two Mach stems induces a high pressure zone. For $\eta = 2.0$, the high pressure zone is concentrated when the central shock wave contacts the interface, driving the formation of a N_2 cavity. As η increases, the high pressure zone is expanded with the maximum pressure magnitude decreasing. Consequently, the N_2 cavity has a smaller penetration depth but a larger area.

The time variations of the geometrical sizes of the interface structure, including the amplitude of the distorted interface (a), the penetration depth of the cavity (h) and the area of the cavity (A), are quantitatively presented in Fig. 7 in which the error bars represent the experimental uncertainty. The schematics

TABLE III. The Mach number of the planar incident shock (Ma), the velocity jump of the shocked interface ($\Delta\upsilon$), the preshock Atwood number (A_t), the slope of the fitted straight line (k) shown in Fig. 7(a), and comparison of the growth rate of the interface amplitude between predicted values ($\dot{a}_{\text{theo}}$) deduced from the Richtmyer's theory and experimental values ($\dot{a}_{\text{exp}}$) obtained in this study.

η	Ma	$\Delta\upsilon$(m/s)	A_t	k	$\dot{a}_{\text{theo}}$ (m/s)	$\dot{a}_{\text{exp}}$ (m/s)
2.0	1.22	76.1	0.68	0.022	16.25	4.68
3.3	1.21	73.0	0.68	0.023	12.47	2.94
4.0	1.23	79.3	0.68	0.021	6.77	2.25

for measuring a, h, and A are indicated in Fig. 5. Note that the cavity area is obtained by measuring the area of all pixels in the cavity. For the case of $\eta = 4.0$, the open edge at the top of the cavity is substituted by a solid edge to create a closed cavity when the area is measured. All the experimental results here are nondimensionalized in the same form. The time and spatial scales are defined as d/V_s and d^2/l, respectively, where V_s is the velocity of the initial planar incident shock wave. It is found in Fig. 7(a) that the dimensionless interface amplitude al/d^2 for each case increases linearly with the dimensionless time tV_s/d, and a collapse is demonstrated for different η numbers in current study. A variation trend similar to al/d^2 is observed for the penetration depth hl/d^2, as shown in Fig. 7(b). As η decreases, the high pressure zone is concentrated when the rippled shock impacts the interface, and, therefore, the penetration depth of the cavity is larger but with a smaller area, as indicated in Fig. 7(c). Note that for the case of $\eta = 2.0$, the dimensionless cavity area $A(l/d^2)^2$ decreases with a quite small reduction rate because a closed cavity is always observed during the time studied. The reduction of the N_2 cavity area is ascribed to the squeeze by the SF_6 gas around the cavity. For the case of $\eta = 3.3$, we can observe from Fig. 5 that at an early stage the cavity is not closed. Squeezed by the surrounding SF_6 gas, the cavity shrinks and becomes closed at a later stage, resulting in a large decrease of the area. For the case of $\eta = 4.0$, an open edge always remains, and owing to the increase of the cavity height, the cavity area also increases.

To quantitatively explore the difference of the instability here and the standard RM instability of a planar shock hitting a perturbed interface, we attempt to equate the preinterface perturbation of the rippled shock in this study with a preshock perturbation of a rippled interface. As indicated in Table II, for all cases, the ratios of a_0/λ_0 are less than 0.1. According to the linear theory proposed by Richtmyer [2], the growth rate of the amplitude $\dot{a}_{\text{theo}}$ can be expressed as

$$\dot{a}_{\text{theo}} = a_0 \frac{2\pi}{\lambda_0} \Delta\upsilon A_t \tag{1}$$

where $\Delta\upsilon$ is the velocity jump of the shocked interface, and A_t is the preshock Atwood number. Based on this model, the theoretical growth rates of amplitude are shown in Table III. Besides, through fitting the evolving amplitude curve into a linear function indicated in Fig. 7(a), the slope k for each case can be obtained. Further, the experimental growth rate of amplitude is calculated using the following expression:

$$\dot{a}_{\text{exp}} = kV_s \frac{d}{l}. \tag{2}$$

From this formula, the experimental growth rates are also given in Table III. Obviously, the theoretical and experimental values are different. For each case, the former is remarkably greater than the latter. The discrepancy indicates that characteristics of this instability are different from those of standard RM instability, which may be ascribed to the pressure nonuniformity behind the incident rippled shock wave.

IV. CONCLUSION

In summary, a rippled shock with three different segments separated by triple points is formed by the incident planar shock diffracting around the rigid cylinder. The segments vary in shape as the shock moves. For a different dimensionless distance η, a nominally flat interface is accelerated by a rippled shock with a different shape, resulting in the diversity of the interface morphology. In general, a "Λ" shaped interface and a cavity are observed after the shock impact. Quantitatively, both the dimensionless interface amplitude and the cavity height increase with the dimensionless time, and reasonable collapses are achieved for different η numbers. Furthermore, through equating the preinterface perturbation of the rippled shock to the preshock perturbation of the perturbed interface, the growth rate of the present instability is found to be much smaller than that of the standard RM instability in the linear stage.

It should be noted that in this work only images of the interface at an early stage are given and analyzed. It is then anticipated that the experiments, coupled with ongoing simulation work, will be able to shed light on the correlations between the pressure behind the rippled shock and the interface morphologies. Moreover, the experiments showing the evolving history of interface perturbation at later stages should be performed to quantitatively investigate the growth of the interface perturbation.

ACKNOWLEDGMENTS

The authors would like to thank Professor Jianfeng Li and Dr. Fangbao Tian for valuable discussion. This work was supported by the National Natural Science Foundation of China (Grants No. 11302201, No. 11472253, and No. 11602247) and the Science Challenge Project (Grant No. JCKY2016212A501).

[1] M. Brouillette, Annu. Rev. Fluid Mech. **34**, 445 (2002).
[2] R. D. Richtmyer, Commun. Pure Appl. Math. **13**, 297 (1960).
[3] E. E. Meshkov, Fluid Dyn. **4**, 101 (1969).
[4] W. D. Arnett, J. N. Bahcall, R. P. Kirshner, and S. E. Woosley, Annu. Rev. Astron. Astrophys. **27**, 629 (1989).
[5] J. Yang, T. Kubota, and E. E. Zukoski, AIAA J. **31**, 854 (1993).
[6] J. D. Lindl, O. Landen, J. Edwards, E. Moses, and NIC Team, Phys. Plasmas **21**, 020501 (2014).
[7] D. Ranjan, J. Oakley, and R. Bonazza, Annu. Rev. Fluid Mech. **43**, 117 (2011).
[8] X. Luo, B. Guan, Z. Zhai, and T. Si, Phys. Rev. E **93**, 023110 (2016).
[9] J. W. Jacobs, Phys. Fluids A **5**, 2239 (1993).
[10] X. Luo, B. Guan, T. Si, Z. Zhai, and X. Wang, Phys. Rev. E **93**, 013101 (2016).
[11] D. Ranjan, M. Anderson, J. Oakley, and R. Bonazza, Phys. Rev. Lett. **94**, 184507 (2005).
[12] C. Mariani, M. Vanderboomgaerde, G. Jourdan, D. Souffland, and L. Houas, Phys. Rev. Lett. **100**, 254503 (2008).
[13] H. Y. Chu and D. K. Chen, Phys. Rev. E **87**, 051002(R) (2013).
[14] C. R. Weber, N. S. Haehn, J. G. Oakley, D. A. Rothamer, and R. Bonazza, J. Fluid Mech. **748**, 457 (2014).
[15] G. C. Orlicz, S. Balasubramanian, P. Vorobieff, and K. P. Prestridge, Phys. Fluids **27**, 114102 (2015).
[16] X. Luo, P. Dong, T. Si, and Z. Zhai, J. Fluid Mech. **802**, 186 (2016).
[17] C. Huete, J. G. Wouchuk, B. Canaud, and A. L. Velikovich, J. Fluid Mech. **700**, 214 (2012).
[18] K. O. Mikaelian, Phys. Rev. Fluids **1**, 033601 (2016).
[19] F. C. Campos and J. G. Wouchuk, Phys. Rev. E **93**, 053111 (2016).
[20] J. W. Grove, R. Holmes, D. H. Sharp, Y. Yang, and Q. Zhang, Phys. Rev. Lett. **71**, 3473 (1993).
[21] J. H. J. Niederhaus, J. A. Greenough, J. G. Oakley, D. Ranjan, M. H. Anderson, and R. Bonazza, J. Fluid Mech. **594**, 85 (2008).
[22] B. J. Olson and J. A. Greenough, Phys. Fluids **26**, 101702 (2014).
[23] J. A. McFarland, D. Reilly, W. Black, J. A. Greenough, and D. Ranjan, Phys. Rev. E **92**, 013023 (2015).
[24] J. X. Xiao, J. S. Bai, and T. Wang, Phys. Rev. E **94**, 013112 (2016).
[25] T. Si, Z. Zhai, and X. Luo, Laser Part. Beams **32**, 343 (2014).
[26] M. Lombardini, D. I. Pullin, and D. I. Meiron, J. Fluid Mech. **748**, 85 (2014).
[27] M. Lombardini, D. I. Pullin, and D. I. Meiron, J. Fluid Mech. **748**, 113 (2014).
[28] L. Biamino, G. Jourdan, C. Mariani, L. Houas, M. Vandenboomgaerde, and D. Souffland, Exp. Fluids **56**, 1 (2015).
[29] T. Si, T. Long, Z. Zhai, and X. Luo, J. Fluid Mech. **784**, 225 (2015).
[30] M. A. Jones and J. W. Jacobs, Phys. Fluids **9**, 3078 (1997).
[31] B. D. Collins and J. W. Jacobs, J. Fluid Mech. **464**, 113 (2002).